A comprehensive study of the electrodeposition of nickel nanostructures from deep eutectic solvents : self-limiting growth by electrolysis of residual water

A Comprehensive Study of the Electrodeposition of Nickel Nanostructures from Deep Eutectic Solvents: Self-Limiting Growth by Electrolysis of Residual Water

El Amine Mernissi Cherigui,[†] Kadir Sentosun,[‡] Pieter Bouckenooge,[†] Hans Vanrompay,[‡] Sara Bals,[‡] Herman Terryn,[†] and Jon Ustarroz*[,†]

†*Vrije Universiteit Brussel, Pleinlaan 2, Research Group Electrochemical and Surface Engineering (SURF), 1050 Brussels, Belgium*

‡*Electron Microscopy for Materials Research (EMAT), University of Antwerp, Groenenborgerlaan 171, B-2020 Antwerp, Belgium*

E-mail: justarro@vub.ac.be

Abstract

The electrodeposition of nickel nanostructures on glassy carbon was investigated in 1:2 choline chloride - urea (1:2 ChCl-U) deep eutectic solvent (DES). By combining electrochemical techniques with ex-situ FE-SEM, XPS, HAADF-STEM and EDX, the electrochemical processes occurring during nickel deposition were better understood. Special attention was given to the interaction between the solvent and the growing nickel nanoparticles. The application of a sufficiently negative potential results into the electrocatlytic hydrolisis of residual water in the DES, which leads to the formation of a mixed layer of $Ni/Ni(OH)_{2(ads)}$. In addition, hydrogen bonds between hydroxide species and the DES components could be formed, quenching the growth of the nickel clusters favouring their aggregation. Due to these processes, a highly dense distribution of nickel nanostructures can be obtained within a wide potential range. Understanding the role of residual water and the interactions at the interface during metal electrodeposition from DESs is essential to produce supported nanostructures in a controllable way for a broad range of applications and technologies.

Introduction

Supported nickel nanoparticles are widely used as catalysts for fuel cells and electrosynthesis, as well as for biosensors and supercapacitors.[1–9] These nanomaterials can be fabricated by multiple methods such as chemical reduction, photochemical synthesis and ionothermal synthesis among others.[10–17] However, electrodeposition offers several advantages since it permits the growth of the nanoparticles directly on the support of interest without the need of surfactants and allows obtaining highly electroactive nanostructures.[18] Nickel nanostructures have been electrodeposited on carbon substrates, from aqueous solutions, using different buffers, such as phosphate,[19] sulfates[20,21] or acetate.[3,22,23] However, the use of aqueous baths for nickel electrodeposition has several drawbacks. On the one hand, nickel cations can be reduced only at highly negative potentials and this leads to a local increase in pH due to the reduction of H^+ species.[20,24,25] Hence, without a pH control, non-soluble nickel hydroxides precipitate in an uncontrollable way, making the reproducibility of the process complicated. Moreover, the structures obtained are often too large and present a broad size distribution. On the other hand, some of these electrolytes require the use of additives to control the electrodeposition process.[26] In recent work, a solution of KCl with H_3BO_3 as buffer and HCl was used in order to control the pH and a homogeneous distribution of small nickel nanoparticles was obtained for very short deposition times.[27,28] Despite this improvement, the presence of hydrogen evolution and the need of using buffered solutions and additives, make the deposition of nickel from aqueous electrolytes challenging.

In this context, Room Temperature Ionic Liquids[29] (RTILs) have been considered as interesting alternatives to aqueous electrolytes for metal electrodeposition, in view of the fact that they offer a wider potential window and a higher stability at higher temperatures. As an exemple, the electrodeposition of nickel nanoparticles from 1-butyl-1-methylpyrrolidinium bis(trifloromethylsulfonyl)amide (BMPTFSA)has been reported.[30] In this case, very small nanostructures were obtained ($\sim$ 3,2 nm) and by adding acetonitrile as additive, the size of the particles was decreased to $\sim$ 1,9 nm. Despite the benefits of the use of RTILs as

deposition baths, their cost is substantially higher and they require to be handled under a controlled,[31] water free, atmosphere. Alternatively, over the last decade, deep eutectic solvents (DESs), a novel type of electrolytes, have generated great enthusiasm among scientists, becoming an alternative to traditional aqueous electrolytes and RTILs. In fact, these eutectics, considered as RTIL analogues, offer many advantages, such as great stability at higher temperatures and broader electrochemical window than aqueous solutions.[32–36] In addition, by using DESs, electrochemical processes can be controlled and slowed down without the need of additives and stabilizing agents. Likewise, these eutectics provide some practical benefits over RTILs, including ease of preparation, lower toxicity and convenient price.[32,35] DESs are known to be highly hygroscopic, being this behavior disadvantageous in some applications.[32] However, the presence of small amounts of water (up to 6 %) in the DES, has recently shown to be beneficial.[37] Moreover, DESs are especially interesting because of their ability to stabilize nanoclusters and to facilitate nanoparticle self-assembly.[38] For these reasons, an increasing number of studies on the electrochemical deposition of nickel from DES have been reported.[39–48] Firstly, nickel electrodeposition from ChCl-U was studied by using an electrochemical quartz microbalance.[39] Furthermore, the electrochemical behaviour of nickel from ChCl-U and ChCl-EG (EG: ethylene glycol) was reported[40] and compared to aqueous solutions.[49] It was shown that nickel deposition can be performed with similar deposition rates from both types of baths. Contrariwise, the morphology of the deposited nickel was different and this dissimilarity was related to the difference of nickel speciation in each media. In addition, electrodeposition from DES has also proven successful to obtain nickel films,[41–43,50] nickel based alloys[44–46] and corrosion resistant nanocrystalline nickel films.[47,48] However, to the best of our knowledge, no studies have been reported on the controlled electrodeposition of nickel nanostructures from any type of DES.

In this paper, we report for the first time on the electrochemical deposition of nickel nanostructures on carbon substrates from ChCl based DESs. Electrochemical techniques are combined with ex-situ FE-SEM, XPS, HAADF-STEM and EDX, to study in detail the

electrochemical processes occurring during nickel deposition. Special attention was given to the interaction between the solvent, the residual water and the electrodeposited nickel phase. This manuscript does not only provide novel information on the electrochemical deposition of nickel in the nanoscale, but also provides important knowledge to benefit from the hygroscopicity of DESs for nanoscale metal deposition.

Experimental

The eutectic solvent was prepared by mixing choline chloride (Sigma-Aldrich, >98%) and urea (Sigma-Aldrich, >99%) in 1:2 molar ratio. Prior to use, choline chloride was recrystallized in absolute ethanol, followed by 12 hours vacuum drying at 80^oC. Urea was only dried under vacuum at 80^oC for 12 hours. The 1:2 ChCl-U mixture was heated at 80^oC for 1 hour and under a constant pressure of nitrogen. $NiCl_2.6H_2O$ was added as received to obtain 10 mM solution. Then, the solution was transferred to the electrochemical cell and kept at 60^oC, under a constant pressure of nitrogen all along the experiments. A Karl Fischer coulometer was used to control the water quantity before each experiment and an average value of (0.08 ± 0.01) $wt\%$ of water was obtained. Cyclic voltammetry (CV), linear sweep voltammetry (LSV) and chonoamperometry (CA) measurements were performed in an electrochemical cell with a three-electrode system, consisting of a silver wire quasi reference electrode (Ag QRE), a platinum counter electrode and a carbon based working electrode. All the potentials mentioned throughout the manuscript refer to Ag QRE. The potential of this reference electrode is known to be stable in this type of DES with high concentration of chlorides.[51] In this work, two types of working electrodes were used: glassy carbon disks (6 mm diameter) and carbon coated TEM grids (CCTGs). Details of the benefits and the use of CCTGs as electrodes can be found elsewhere.[52,53] Before each experiment, the glassy carbon working electrode was polished with 0.3 μm alumina paste, sonicated twice for 5 min in Milli-Q water and absolute ethanol. Carbon coated TEM grid electrodes were used

as received. Prior to the characterization of the nickel deposit, the carbon electrodes were cleaned with water and ethanol to eliminate the residual solvent.

The electrochemical measurements were handled by a computer controlled Autolab PGSTAT12. Signal imposing and data acquisition were carried out by NOVA 1.10.5 software. Scanning electron imaging was performed by a JEOL JSM-7100F field emission scanning electron microscope (FE-SEM), operated at acceleration voltages of 15 kV and 20 kV. X-ray photoelectron spectroscopy (XPS) measurements were carried out using a PHI-5600ci with an Al filament emitting X-rays at 1486.6 keV. High angle annular dark field scanning transmission electron microscopy (HAADF-STEM) images were acquired using an aberration corrected electron microscope (cubed FEI Titan 60300), operated at 300 kV. Energy-dispersive X-ray spectroscopy (EDX) maps were acquired in the transmission electron microscope using a ChemiSTEM system whereas the analysis was performed using the Bruker ESPRIT software.

Results and discussion

1. Electrochemical Measurements

A cyclic voltammogram recorded on glassy carbon from 1:2 ChCl-U containing 10 mM $NiCl_2$, at 60 ^0C, is shown in Figure 1 together with a cyclic voltammogram of 1:2 ChCl-U (blank). The voltammogram of the nickel containing mixture exhibits different cathodic and anodic responses. The cathodic waves are coded R_1, R_2 and R_3 with onsets at E = -0.72 V, E = -1.03 V and E = -1.15 V, respectively. The anodic responses are coded O_1, O_2 and O_3 with the potentials at maximum current recorded at E = -0.35 V, E = -0.02 V and E = +0.19 V, respectively. It is important to notice that for the waves O_1 and O_2, the involved currents are difficult to assign due to their broadness. These acronyms will be used hereafter when referring to the cathodic and anodic processes.

According to previous studies,[39–42] the cathodic wave R_1 can be attributed to the reduc-

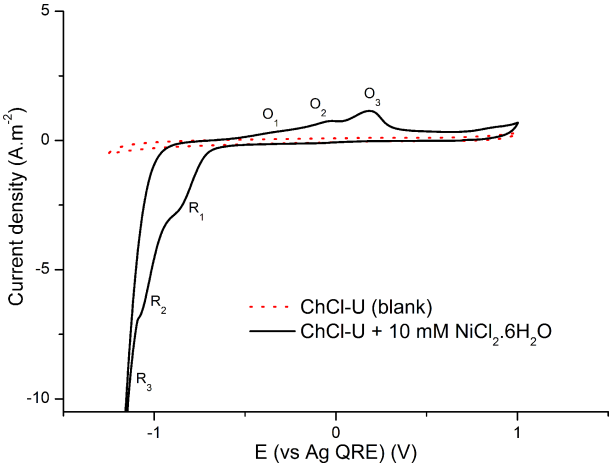

Figure 1: Cyclic voltammograms of 1:2 ChCl-U (blank) and 1:2 ChCl-U containing 10mM of $NiCl_2$-$6H_2O$ recorded on GC. $\nu = 50$ mV/s. $T = 60^oC$.

tion of Ni^{2+} to Ni. R_3 can be assigned to a cathodic breakdown, that is catalysed by the deposited nickel on the surface of the electrode. The three oxidation responses have so far been attributed to the stripping of two different morphologies of the nickel deposit. This ascription was based on former studies about the electrodeposition of zinc from DESs.[40,54] To have a better understanding of the electrochemical responses, different experiments were undertaken. Figure 2 (a) shows different LSVs recorded after deposition for 120 s at different potentials close to R_1 and R_2, i.e., at E = -0,72 V (green curve), E = -0.8 V (blue curve), E = -0.9 V (black curve) and at E = -1,1 V (red curve). For depositions at less negative potentials (R_1 : green, blue and black curves), the subsequent LSVs show a small (O_2) and a large (O_3) anodic waves. However, for depositions at more negative potentials (R_2 : red curve), the recorded LSV features much smaller anodic peak O_3, an increase of the charge of O_1 and a shift of O_2 to a more negative potential, referred to as O'_2, with wave potential at E = -0,18 V. In the latter case, the LSV shows also the beginning of an additional anodic wave starting at E = +0.52 V. The total charge densities recorded from the chronoamperograms of these depositions are reported in Figure S1 of the supporting information. The charge densities are increasing (absolute values) for depositions at more negative potentials.

To further elucidate the nature of the anodic responses O_1, O_2 and O_3, potentiostatic

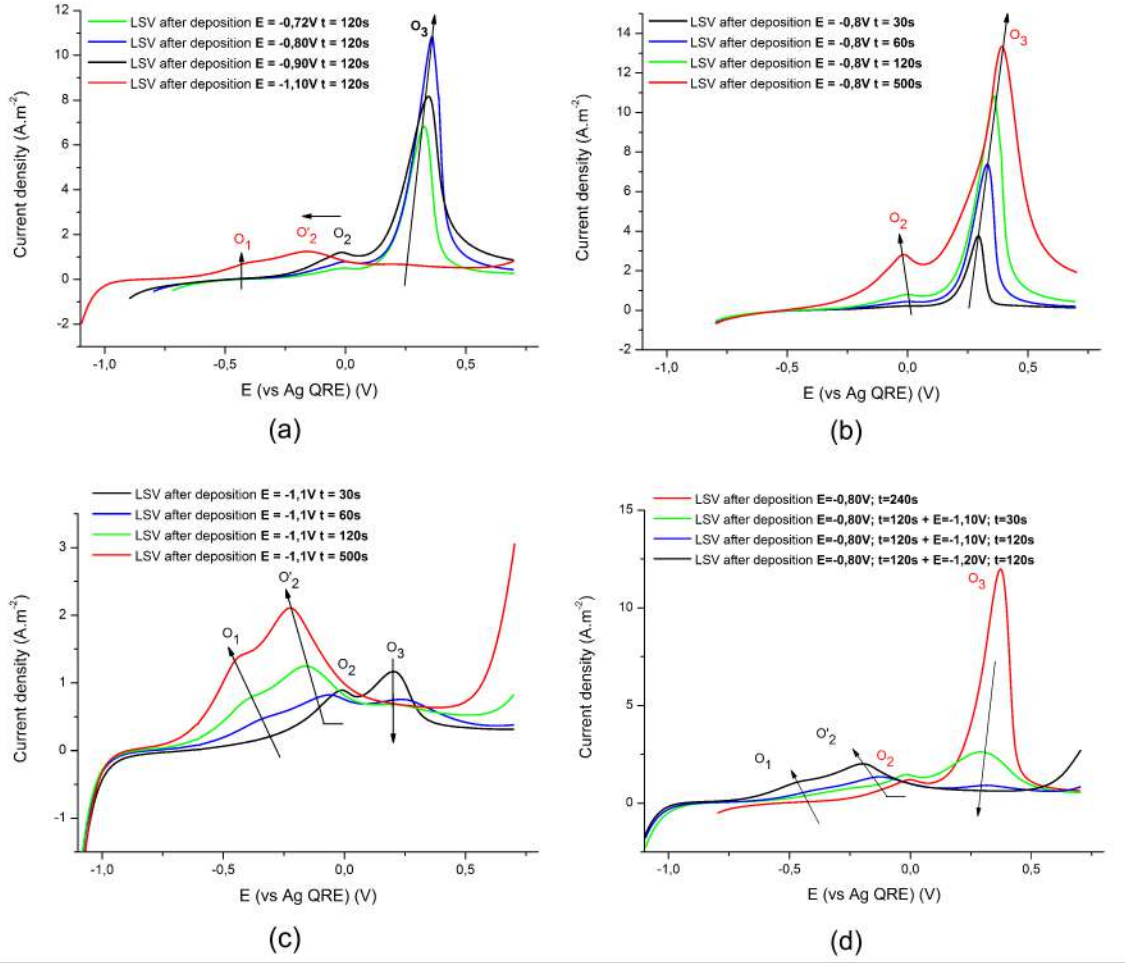

Figure 2: LSV recorded on GC in a solution of 1:2 ChCl-U containing 10mM of $NiCl_2$-$6H_2O$ after a potentiostatic deposition of nickel (a) for 120 s at E = -0,72 V (green curve), E = -0,8 V (blue curve), E = -0,9 V (black curve) and E = -1,1 V (red curve); (b) at E = -0,8 V for 30 s (black curve), 60 s (blue curve), 120 s (green curve) and 500 s (red curve); (c) at E = -1,1 V for 30 s (black curve), 60 s (blue curve), 120 s (green curve) and 500 s (red curve); (d) at E = -0,8 V for 240 s (red curve), at E = -0,8 V for 120 s followed by another pulse at E = -1,1 V for 30 s (green curve) or for 120 s (blue curve) and at E = -0,8 V for 120 s followed by another pulse at E = -1,2 V (black curve). ν = 50 mV/s, $T = 60^oC$.

electrodeposition followed by LSV was conducted for variuos times at two different potentials. Figure 2 (b) shows LSVs recorded after an initial deposition at E = -0.8 V (R_1) for different times. The increase of deposition time induces an increase of the charge $Q(O_3)$ and to a lesser extent the charge $Q(O_2)$. This confirms that there is a direct relationship between the first reduction (R_1) and the third anodic (O_3) processes. This anodic process corresponds to the stripping of nickel deposited during the polarisation at R_1 (further discussed in section 2 after FE-SEM analysis). In the same way, Figure 2 (c) shows LSVs recorded after an initial polarisation for different times at E = -1,1 V (R_2). On the one hand, the charge of the stripping $Q(O_3)$ decreases with the increase of polarisation time. On the other hand, the charge $Q(O_1)$ increases with polarisation time. Likewise, the process O_2 shifts to more negative potentials (O'_2) and its associated charge increases. It can be concluded that the process R_2 inhibits the stripping of nickel and enhances the anodic responses O_1 and O_2. These effects are intensified when the duration of the process R_2 increases. Moreover, an additional anodic wave appears at more positive potentials ($E > +0,5$ V) and its intensity increases with polarisation time.

Figure 2 (d) shows LSVs recorded after an initial deposition of 120 s at E = -0,8 V followed by a second potentiostatic polarisation at E = -1,1 V (blue and green curves) or at E = -1,2 V (black curve). These LSVs were compared to another one recorded after deposition at E = -0,8 V for 240 s (red curve). In the cases that a second pulse is applied at E = -1,1 V (blue and green curves), the anodic processes O_1 and O'_2 occur and their associated charge increases with the duration of the second pulse (30 s and 120 s), unlike O_3, whose current density decreases drastically. When the second pulse is more negative (E = -1,2 V), the charges $Q(O_1)$ and $Q(O'_2)$ are higher. Contrariwise, the process O_3 disappears completely. In the latter case, as shown in Figure 2 (c), an anodic wave appears at more positive potentials ($E > +0,5$ V). It can be deduced that both O_1 and O'_2 are anodic processes which only occur when the cathodic process R_2 has taken place beforehand. Furthermore, the cathodic process R_2 followed by O_1 and O_2, passivate the surface of the

deposited nickel against anodic stripping. The extent of these processes depends on the applied potential and its duration. Further discussion is given in section 2.

To understand the effect of the anodic processes on subsequent nickel electrodeposition, the CVs shown in Figure 3 (a) were conducted. Potentiostatic depositions at R_1 and R_2 followed by an anodic sweep up to $E = +0{,}7$ V (Figure 3 (a), bold curves) were subsequently followed by cathodic sweeps (Figure 3 (a), dashed curves). After deposition at R_1 and the subsequent anodic sweep, the following cathodic sweep shows a reduction wave starting at E = -0,35 V (dashed red curve) which corresponds to the deposition of nickel. On the other hand, the cathodic sweep after deposition at E = -1,1 V and the subsequent anodic sweep (dashed black curve), shows no reduction, resulting probably from the passivation of the whole electrode surface, i.e. the glassy carbon and the previously deposited Ni phase. It can be deduced that deposition at R_2 for long times followed by the anodic processes O_1 and O'_2 causes further nickel growth to be inhibited.

Moreover, an anodic sweep after deposition at E = -1,1 V followed by 300 s resting time at open circuit potential (OCP) was also conducted (Figure 3 (b)). The anodic sweep of the CV (bold blue curve) shows surprisingly a strong anodic peak O_3, corresponding to the stripping of Ni. The reverse cathodic sweep recorded subsequently (dashed blue curve) shows, for its part, a reduction wave corresponding to the deposition of Ni. No inhibition of Ni stripping, neither of further Ni growth are observed in these conditions. Hence, the surface is passivated only if nickel deposition occurs at very negative potentials (R_2) and anodic polarisation is applied directly afterwards.

In addition, as highlighted before, when Ni is deposited at highly negative potentials for long times, the LSV recorded afterwards shows an anodic wave starting at $E = +0{,}52$ V. In Figure 3 (c), a cyclic voltammogram with a higher anodic limit ($E = +1{,}5$ V) is shown. In the first scan, an additional anodic wave at $E = +0{,}98$ V (hereafter referred to as O_4) is shown. Further cycling between these limits results into a drastic decrease of the charge associated to this process (O_4). Contrariwise, O_2 and O_3 increase progressively with the following scans.

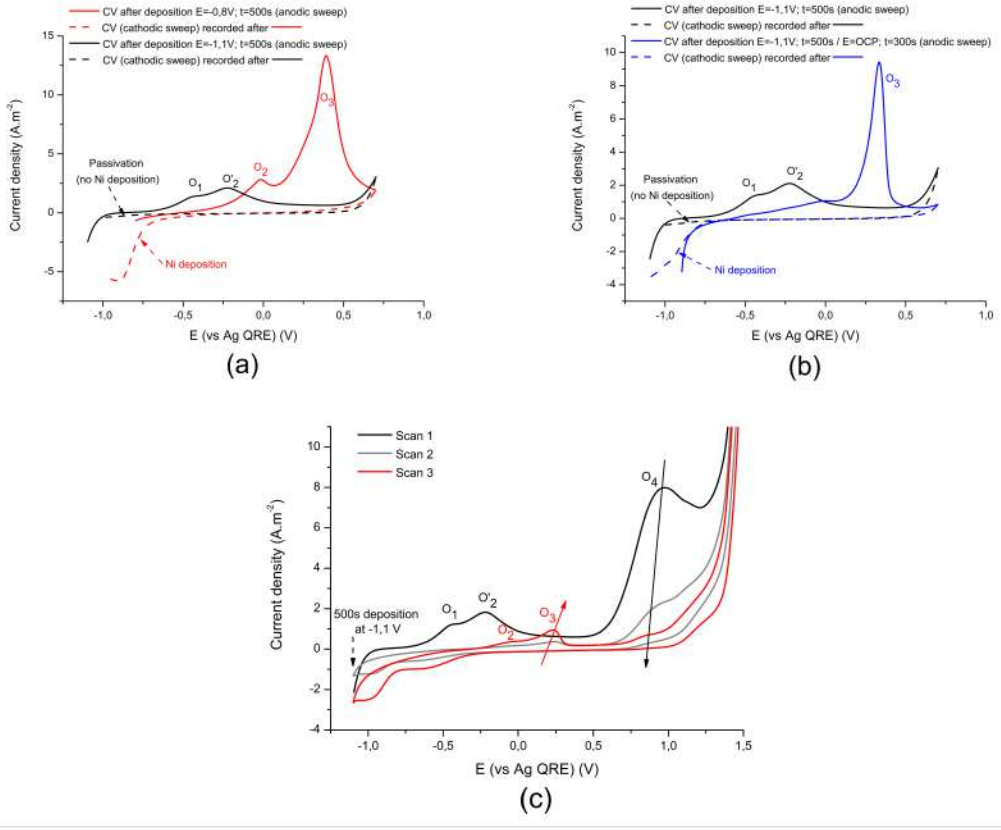

Figure 3: CV recorded on GC in a solution of 1:2 ChCl-U containing 10mM of $NiCl_2$-$6H_2O$ after a potentiostatic deposition of nickel (a) for 500s at E = -0,8 V (red curve) and at E = -1,1 V (black curve); (b) for 500 s at E = -1,1 V (black curve), and for 500 s at E = -1,1 V followed by 300 s resting time at the OCP (blue curve). The potential was subsequently swept from the deposition potentials in the positive direction (continuous lines) and then to the negative potentials (dashed lines). (c) CVs recorded on GC after a potentiostatic deposition of the nickel at E = -1,1 V during 500 s. The potential was subsequently swept from the deposition potentials in the positive direction. ν = 50 mV/s. $T = 60^oC$.

This indicates that the anodic process O_4 results into a gradual depassivation of the surface that allows nickel to be stripped off and redeposited on the electrode. Further discussion is provided in section 2.

2. FE-SEM characterization

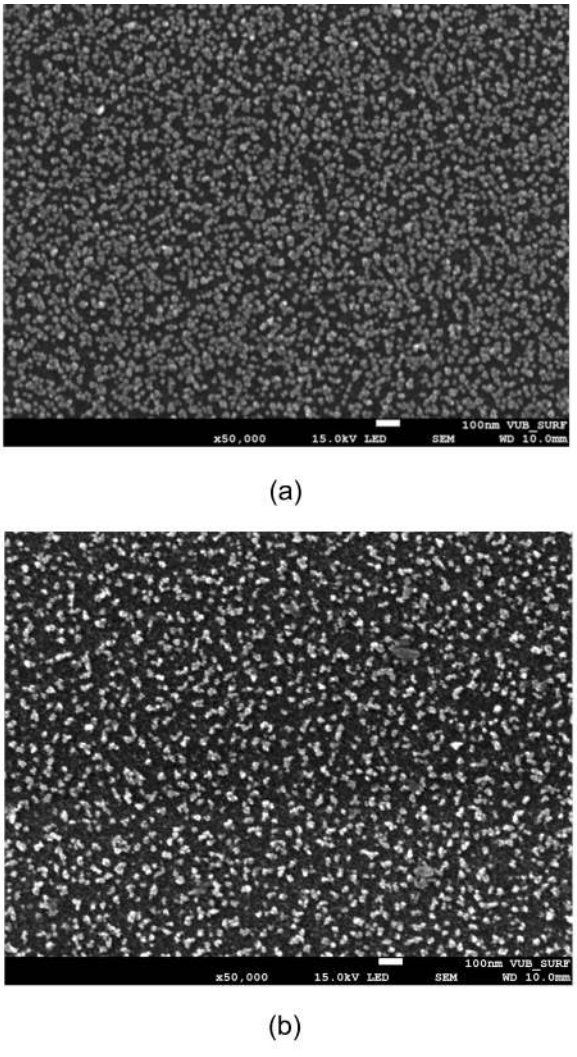

Figure 4: FE-SEM images of the nickel nanostructures deposited from 1:2 ChCl-U on GC for 500 s at (a) E = -0,8 V, Q = -390.9 C/m^2 and (b) E = -1,1 V, Q = -1486.7 C/m^2.

Before all the experiments described below, an electrochemical pre-treatment of the electrode was carried out at $E = +0.7$ V for 120 s in order to avoid spontaneous nickel deposition. Figure 4 shows representative FE-SEM images of nickel nanostructures deposited for 500 s

from 1:2 ChCl-U on GC. The deposition potentials were E = -0,8 V (Figure 4 (a)) and E = -1,1 V (Figure 4 (b)). When E = -0,8 V, a dense and homogeneous distribution of small NPs ($\phi < 50$ nm) is obtained. The total amount of charge involved in this process is Q = -390,9 C/m^2. Contrariwise, for E = -1,1 V, a less dense and less homogeneous distribution of NPs is observed. The total charge involved during this deposition is much higher and corresponds to Q = - 1486,7 C/m^2. The increase of the total charge as well as the decrease of the amount of electrodeposited Ni, as shown in figure 4, are related to the parallel electrochemical processes occurring at highly negative potentials (R_2) that compete and hence, hinder Ni electrodeposition (see Figure 3 (a) and discussion thereafter).

Moreover, double pulse experiments were carried out in order to evaluate the effect of the anodic processes. Figure 5 (a) shows a FE-SEM image of Ni NPs deposited at E = -0,8 V for 500 s followed by an anodic pulse for 500 s at E = 0,0 V corresponding to the potential at which the anodic wave O_2 has the maximum current. Ni NPs remain on the electrode. This further confirms that the anodic wave O_2 does not correspond to the stripping process. On the other hand, Figure 5 (b) shows a FE-SEM image corresponding to a similar experiment in which the second pulse corresponds this time to E = +0,5 V, a potential slightly more positive than the one corresponding to the peak O_3 and where the Ni NPs should be stripped according to the CVs / LSVs. The FE-SEM image shows that Ni NPs have been stripped completely, confirming that the anodic response O_3 is, indeed, the oxidative dissolution of metallic Ni. Likewise, Figures 5 (c) and 5 (d) represent depositions carried out at E = -1,1 V followed by anodic pulses for 500 s at E = -0,23 V corresponding to the potential at which the anodic wave O'$_2$ has the maximum current and E = +0,5 V corresponding to the current peak of O_3, respectively. In both cases, a large number of Ni NPs remain on the surface of the electrode. Unlike the previous case (Figure 5 (b)), if cathodic deposition of nickel occurs at E = -1,1 V, the deposited nanostructures are not completely stripped off at E = +0,5 V. It is therefore confirmed that the anodic processes O_1 and O'$_2$ do not correspond to the stripping of the deposited nickel. Contrariwise, depositing nickel at E = -1,1 V, followed

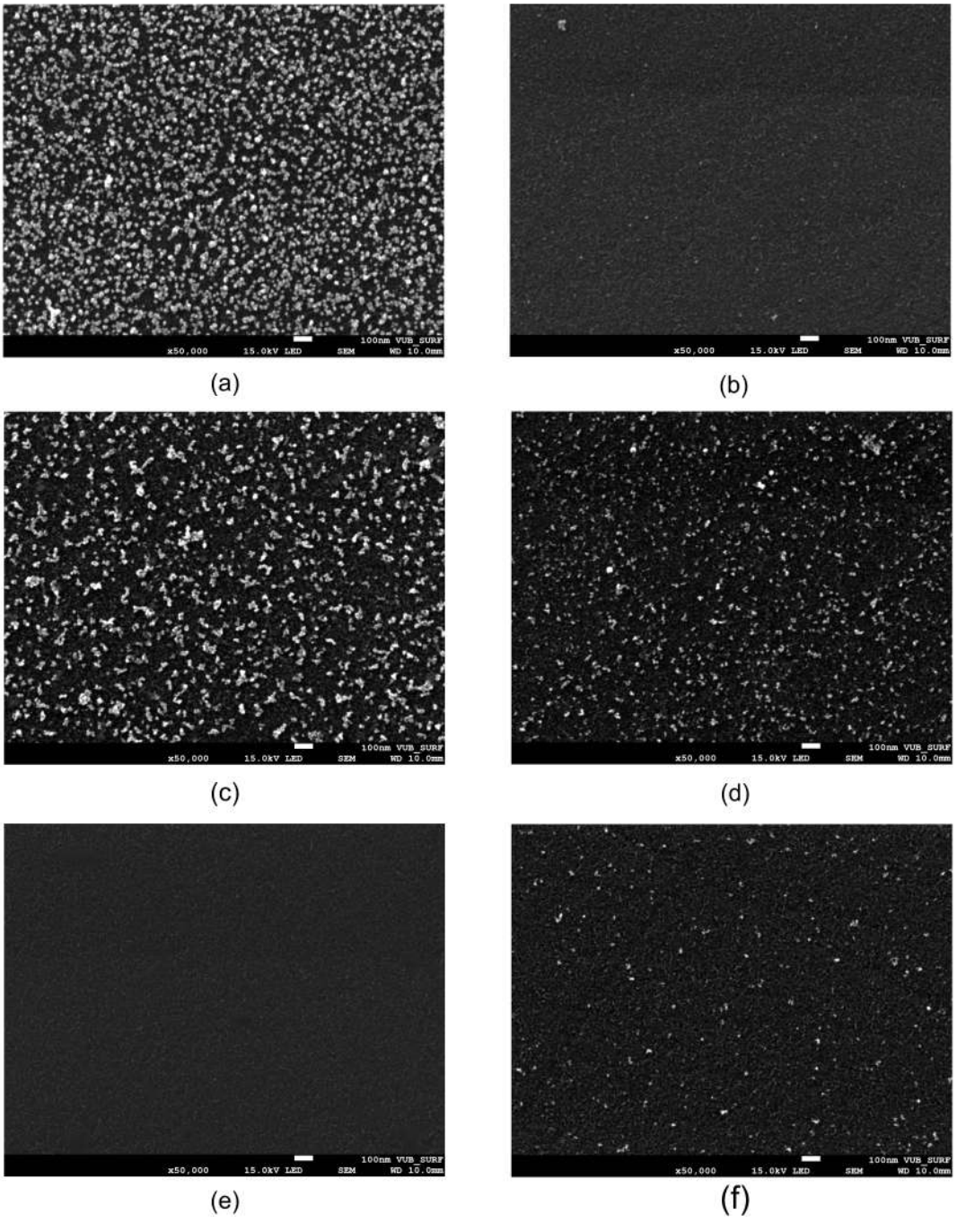

Figure 5: FE-SEM images of the surface of the electrode after a double potentiostatic pulse (500 s each) (a) E_1 = -0,8 V and E_2 = 0,0 V (b) E_1 = -0,8 V and E_2 = 0,5 V, (c) E_1 = -1,1 V and E_2 = -0,23 V, (d) E_1 = -1,1 V and E_2 = +0,5 V, (e) E_1 = -1,1 V and E_2 = +0,98 V, and (f) E_1 = -1,1 V and E_2 = +0,5 V with 300 s resting at OCP between the two pulses.

by an anodic pulse at E = +0,98 V (corresponding to the potential at which the anodic wave O_4 has the maximum current), results into a nickel-free surface as shown in Figure 5 (e). It can be concluded that the more positive anodic process O_4 leads to the oxidative electrodissolution of the nickel deposit. Figure 5 (f) shows a representative FE-SEM image corresponding to a deposition at E = -1,1 V followed by 300 s resting time at OCP and followed by a second potentiostatic pulse (500 s) at E = +0,5 V. Almost no nickel remains at the surface. This is in good agreement with the voltammetric results shown previously (see Figure 3 (b)), which indicate that anodic passivation only occurs when a highly negative potential (R_2) is followed immediately by anodic polarization.

3. TEM characterization

A recent approach, based on using carbon coated TEM grids as electrochemical electrodes, was used to study, at the atomic scale, the electrodeposited structures directly from the electrode. This technique permits the study of the supported as-electrodeposited nanostructures, by transmission electron microscope without the need of removing the nanoparticles from the surface.[52,53]

Figures 6(a) and 6(b) show high resolution HAADF-STEM images acquired after deposition at E = -0,9 V for 60 s. Low resolution HAADF-STEM images are shown in Figure S1(a)of the supporting information. The contrast differences indicated by a blue and red arrow in Figure 6(a) suggest the formation of a core-shell structure. Moreover, ultra small crystalline particles are present all over the carbon grid. The coexistence of ultra-small clusters with larger aggregates has been reported on several occasions for metal electrodeposition on carbon from aqueous[53,55–57] and non-aqueous electrolytes.[38] As illustrated by the HAADF-STEM image in Figure 6(b) and the Fast Fourier Transform (FFT) presented as an inset, both the core and the shell are crystalline. The measured d values from the FFT are in strong agreement with metallic Ni and NiO. These observations suggest a Ni core surrounded by a NiO shell. These observations are confirmed by the EDX maps presented

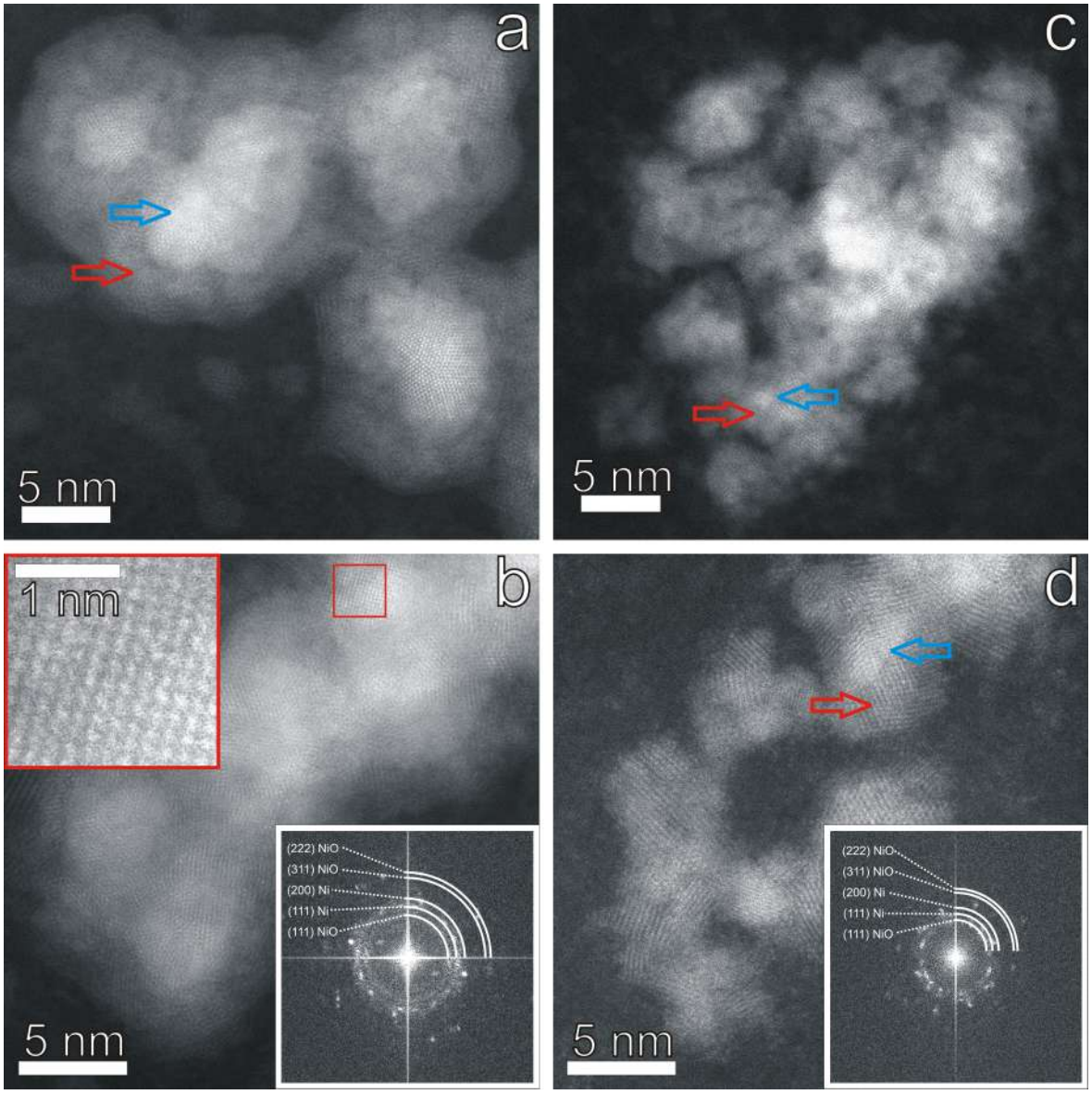

Figure 6: HAADF-STEM micrographs of Ni nanoparticles after deposition for 60 s (a) and (b) at E = -0,9 V and (c) and (d) at E = -1,1 V.

in Figures 7 (a) and (b). The Ni content is found to be homogeneous across the nanoparticle whereas the O content is higher at the edges.

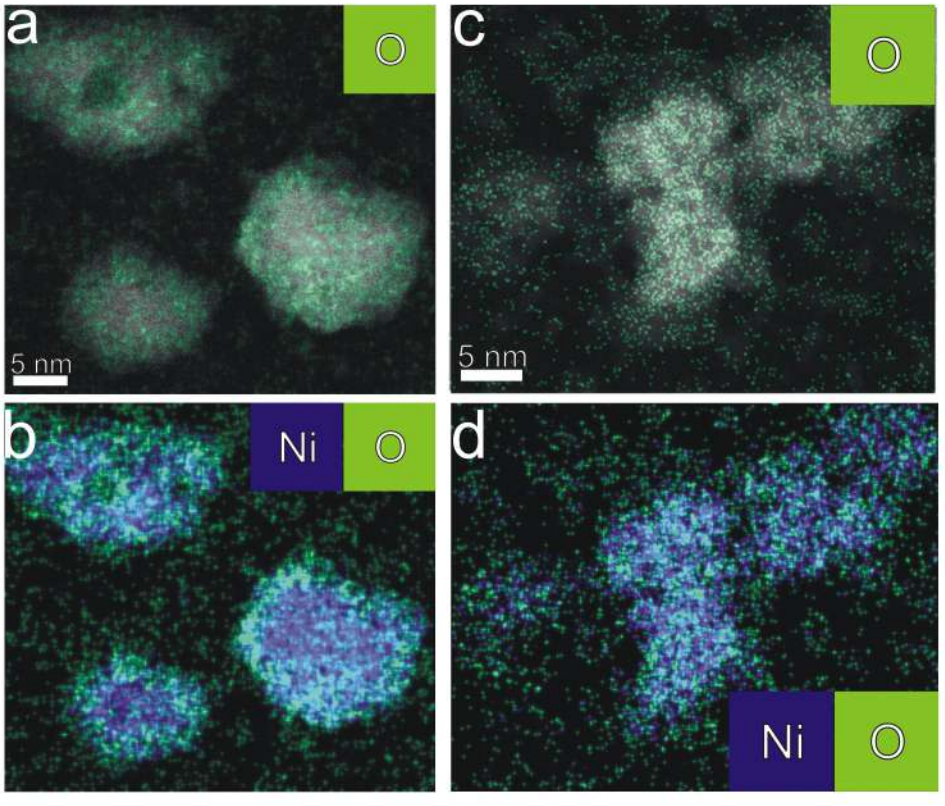

Figure 7: EDX map results for Ni deposited for 60 s at (a) and (b) E = -0,9 V and (c) and (d) E = -1,1 V. (a) and (c) The overlay between HAADF image and O map. (b) and (d) The overlay between the Ni map and O map.

Figures 6(c) and 6(d) display high resolution HAADF-STEM images recorded after deposition at E = -1,1 V for 60 s. Low resolution HAADF-STEM images are shown in Figure S1(b)of the supporting information. The HAADF-STEM image reveals that the nanoparticles consist of agglomerated cristallites with dimensions from 3 to 7 nm. The core-shell structure is not as prominent as the previous case. As highlighted with arrows in Figures 6(c) and (d), contrast difference suggests the presence of Ni in the core and NiO as matrix. Again, HAADF-STEM imaging (Figure 6(d)) and corresponding FFT reveals the crystallinity of the sample with d values corresponding to the metallic Ni and NiO. Also, a

highly dense distribution of ultra small clusters ($\phi < 1$ nm) around the larger clusters could easily be observed. A representative EDX map from this sample is presented in Figures 7 (c) and (d). The EDX map shows that the oxygen presence is homogeneous across the nanoparticles. These results suggest that the amount of metallic Ni after applying E = -1,1 V is smaller than this obtained after applying E = -0,9 V, and it is surrounded by an oxidized form of Ni.

4. XPS characterization

To obtain further chemical information of the surface of the deposited nickel, XPS characterization was carried out. Figure 8 (a) shows the XPS multiplex obtained after depositing Ni at E = -0,9 V for 120 s. This multiplex corresponds to the binding energies between E_{be} = 845 eV and E_{be} = 895 eV, which include the peaks Ni 2P1 and Ni 2P3 for Ni. The Ni 2P3 with binding energy E_{be} = 852,7 eV corresponds to the metallic form of Ni, whereas the transition with binding energy of E_{be} = 856 eV is typically related to the chemical signature of nickel oxi/hydroxide (NiO / $Ni(OH)_2$).[58–61] The biding signals at E_{be} = 862 eV and E_{be} = 884 eV can be attributed to the shake-up peaks (multielectron excitation).[58,59] When a more negative potential is applied (E = -1,1 V), the Ni 2P multiplex (Figure 8 (b)) shows that the signature of the nickel oxi/hydroxide is predominant compared to the metallic form. Finally, Figures 8 (c) and 8 (d) show XPS multiplexes of both samples prepared at E = -0,9 V and E = -1,1 V, respectively, recorded after sputtering approximately a thickness of 1 nm. Only metallic Ni (Ni 2P3 at E_{be} = 853 eV), remains on the glassy carbon surface.

These results, evidence that the nanoparticles are formed by a metallic nickel core and a thin shell of nickel oxi/hydroxide. This multilayer structure is known to be formed on the surface of metallic nickel exposed to water and air.[58,59,62,63] Despite the fact that all the samples were handled and cleaned in the same way, the signature of nickel oxi/hydroxide is largely predominant at the surface of the nanoparticles electrodeposited at E = -1,1 V (R_2). This is explained as follows: at more negative potentials, residual H_2O in the DES reduces to

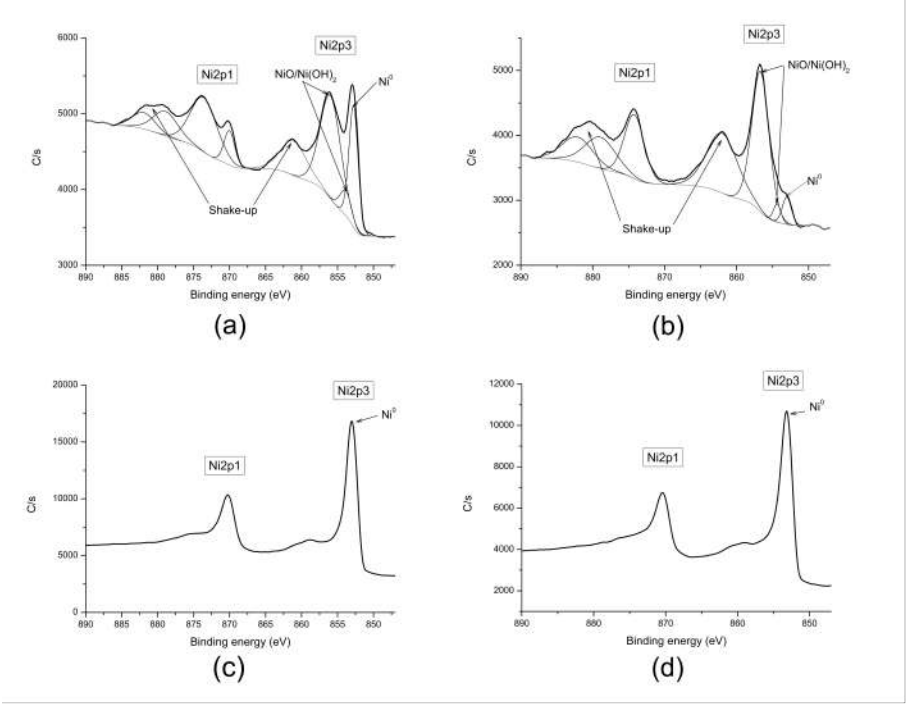

Figure 8: XPS multiplex after deposition at E = -0,9 V for 120 s of Ni2p (a) before and (c) after sputtering; and deposition at E = -1,1 V for 120 s of Ni2p (b) before and (d) after sputtering. Depositions were conducted from 1:2 ChCl-U + 10 mM $NiCl_2$-$6H_2O$ on GC at $T = 60^oC$.

H_2 and OH^-. The later can react with Ni^{2+}, present at the interface, precipitating as nickel hydroxide at the surface of the electrode. The interrelation of the electrochemical processes occuring during the electrochemical growth of Ni from DES, is discussed in the following section.

Discussion

FE-SEM, XPS, TEM, and EDX characterization were combined with electrochemical experiments to gain a better understanding of the electrochemical processes occurring during nickel deposition from 1:2 choline chloride urea deep eutectic solvent. The electrochemical responses R_1 and O_3 (Figure 1) can certainly be attributed, FE-SEM images as support, to the reduction of Ni^{2+} (Eq. (1)) and the stripping of Ni (Eq. (2)), respectively:

$$Ni^{2+} + 2e^- \rightarrow Ni \tag{1}$$

$$Ni \rightarrow Ni^{2+} + 2e^- \tag{2}$$

Electrodeposited Ni nanoparticles at two different potentials, R_1 and R_2, were characterised using FE-SEM and TEM. In both cases, a dense and homogeneous distribution of small nanostructures is obtained. Besides, high resolution HAADF-STEM images highlight the poly-crystallinity of these particles and reveal the presence of very small crystalline nanoclusters. This implies that progressive nucleation and aggregation are favored and growth by direct attachment of nickel is limited. This can be related to the formation of a passivation layer, especially at highly negative potentials. This behavior was already reported in this type of DES during the electrodeposition of Pd NPs from 1:2 ChCl-U. By using in-situ synchrotron ultra small angle X-ray scattering (USAXS) and electrochemical impedance spectroscopy (EIS), the nanoparticles were shown to assemble into 2-D superstructures, rich in adsorbed species. These superstructures could induce the formation of an anionic layer above the NPs.[38,64] Most likely, at highly negative potentials, a competing electrochemical

process (R_2) limits the growth by direct attachment favouring nanocluster aggregation.[53,55] This is in line with adsorption of H on Pt[53,65] and of OH on Fe-group metals[66] being self-terminating growth processes during electrodeposition from aqueous solutions.

As evinced previously for the anodic responses O_1 and O'_2 to take place, they must be immediately preceded by the cathodic reaction R_2. It was shown that only the concatenation of these three processes leads to the inhibition of nickel stripping and the passivation of the electrode surface for further nickel electrodeposition.

The inferred processes are discussed along the schematic representation shown in Figure 9 (a) and (b). A likely explanation is that the residual water, present in the DES, is reduced to H_2 and OH^- (Eq. (3)). This reduction is catalysed by the electrodeposited nickel.[66] The hydroxide anions formed at the surface of the electrode can react with Ni^{2+} from the solvent and precipitate as nickel hydroxide on the surface of the electrode (Eq. (4)):

$$2H_2O + 2e^- \rightarrow H_2 + 2OH^- \tag{3}$$

$$Ni^{2+} + 2OH^- \rightarrow Ni(OH)_{2(ads)} \tag{4}$$

A mixed $Ni/Ni(OH)_{2(ads)}$ layer will be then formed at the surface of the nickel nanoparticles leading to the passivation of the Ni NPs from further growth. A similar hydroxide blocking effect was also suggested in recent studies on nickel electrodeposition from aqueous solutions.[27,66,67] It must be born in mind that the amount of H_2O available is very small when compared to aqueous solutions. Due to that, equations (3) and (4) result into the formation of a thin layer instead of the uncontrollable precipitation occurring in aqueous electrolytes. Hydrogen bonds could be formed between these hydroxide species and the DES components, i.e. urea and choline chloride, as schematically illustrated in Figure 9 (c). These processes could explain the passivation phenomena observed at more negative potentials. Once polarization is stopped and no more OH^- is generated, the OH^- / DES complexes would diffuse away from the interface leading to the depassivation behaviour described in Figure3 (b) and

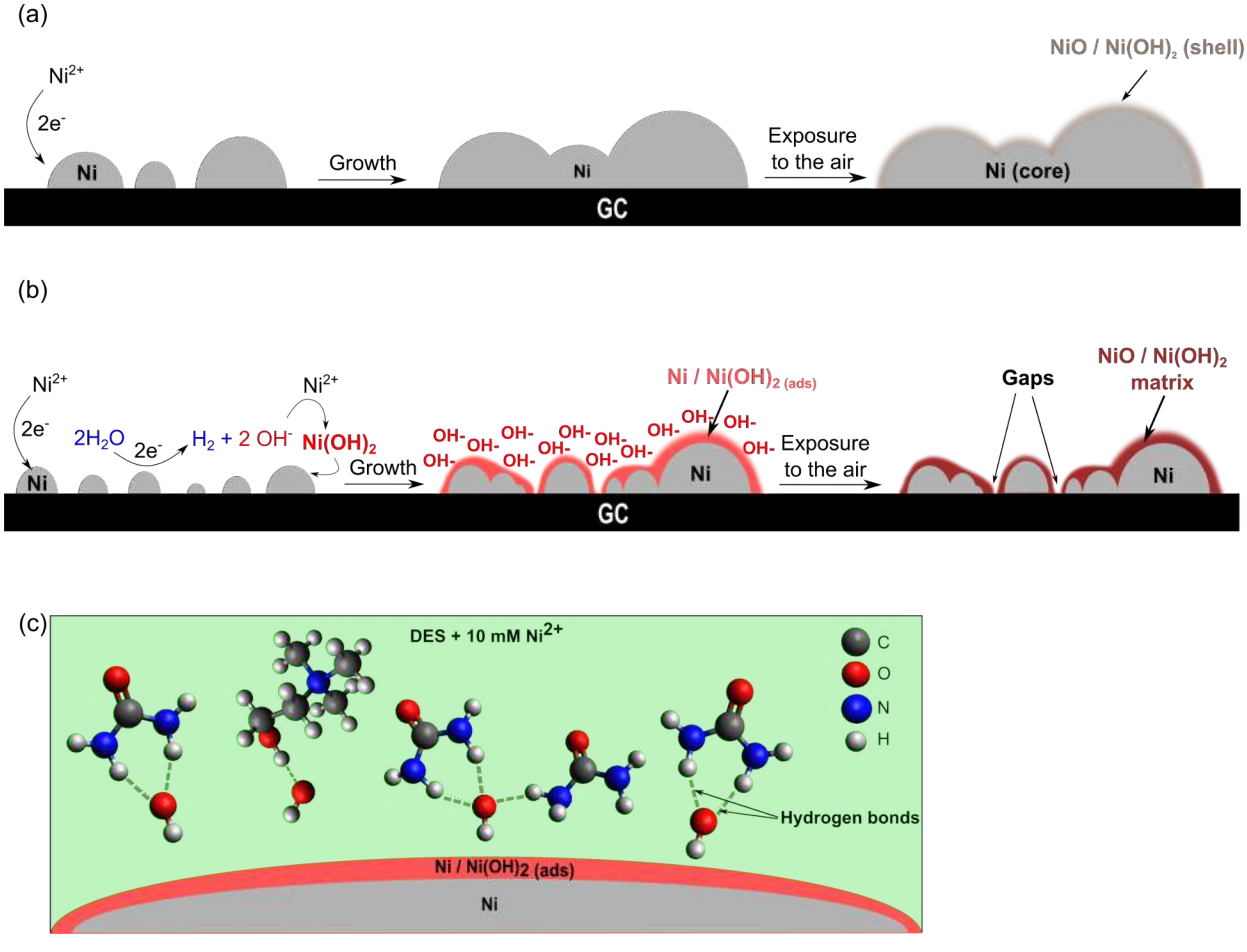

Figure 9: Scheme of the electrochemical processes occurring at (a) R_1 and (b) R_2. (c) Hydrogen bonds formed between hydroxides and DES components (urea and choline chloride).

discussion therein.

The inhibition of the nickel stripping, during anodic polarisation, for the nanostructures formed at highly negative potentials, as shown in Figure 2 (c), is attributed to the anodic formation of $Ni(OH)_2$ by the reaction of Ni (Eq. (5)) or $Ni(OH)_{ads}$ (Eq. (6)) with OH^- present at the surface:[68]

$$Ni + OH^- \rightarrow Ni(OH)_{(ads)} + 1e^- \tag{5}$$

$$Ni(OH)_{(ads)} + OH^- \rightarrow Ni(OH)_{2(ads)} + 1e^- \tag{6}$$

These processes are attributed to the anodic responses O_1 and O'_2, respectively, and they are enhanced by the presence of the precipitated $Ni(OH)_{2(ads)}$ on the surface of Ni NPs. In fact, the boundary between $Ni(OH)_{2(ads)}$ and Ni could be beneficial for further nickel hydroxide formation.[67] Once the surface of the nanostructures is composed exclusively of nickel hydroxide, no stripping of metallic Ni occurs, i.e absence of the response O_3 in Figure 2 (c). Furthermore, this hydroxide layer ($Ni(OH)_{2(ads)}$ and OH^- / DES complexes) prevents further nickel deposition as shown in Figure 3 (a). When the potential is swept to more positive potentials (Figure 3 (c)), the anodic response O_4 can be attributed to the oxygen evolution reaction coupled with an oxidative electrodissolution of $Ni(OH)_2$ (Eq. (7)) and it is consistent with the most generally accepted mechanism involving the adsorption of hydroxides and the generation of dioxygen.[69] This can occur because the hydroxide anions are present in excess and are stabilised at the electrode/electrolyte interface (Figure 9 (b) and 9 (c)).

$$Ni(OH)_2 + 2OH^- \rightarrow O_2 + 2H_2O + Ni^{2+} + 4e^- \tag{7}$$

At this range of positive potentials (O_4), the partial oxidation of the $Ni(OH)_{2(ads)}$ to form NiOOH is also plausible.

$$Ni(OH)_2 + OH^- \rightarrow NiOOH + H_2O + e^- \tag{8}$$

The exponential increase of the current around $E = +1.25$ V, could be explained by an anodic breakdown of the DES. Chlorine formation at this range of potentials has been reported previously in this type of DES.[70] When the hydroxide anions present at the interface are oxidized, further deposition of nickel is possible. The anodic stripping is also no longer inhibited, as shown in Figure 3 (c) (scans 2 and 3), due to the removal of the passivation layer.

It is important to notice that for long depositions at R_1, where only nickel deposition is supposed to occur, the anodic process O_2 appears in the LSV (red curve in Figure 2 (a)) recorded just after the deposition and it is accompanied by a shift of the stripping peak (O_3) towards a more positive potential. We can attribute this effect to the electrochemical processes described in Eq. (5) and (6). In fact, a dense and homogeneous distribution of deposited Ni nanostructures can lead to the catalytic electrolysis of water, but in a lesser extent, compared to when more negative potentials are applied. The small amount of hydroxide anions generated at the interface does not allow the entire surface to be covered by nickel hydroxide and hence, Ni stripping and further Ni growth is possible as highlighted in the red curves (solid and dashed) of Figure 3 (a).

In addition, FFT coupled with HRTEM, and EDX analysis underscored the core-shell structure of the nanoparticles deposited at potentials close to R_1 with metallic Ni as core and NiO composite as shell with a high concentration of oxygen at the edges (Figures 7 (a) and (b)). In the case of NPs deposited at potentials close to R_2, they consist of more complex and mixed structures of poly-cristalline Ni and NiO. As explained before, at more negative potentials, the passivation phenomenon leads to the quenching of metal growth at the early stage and the aggregation of very small clusters. This may explain the gaps that are present within the structures and also the homogeneous presence of oxygen throughout the NPs as shown by EDX (Figures 7 (c) and (d)). Contrary to XPS analysis, the FFT analysis does not reveal the presence of nickel hydroxide. This can be explained by the disordered structure of $Ni(OH)_2$ precipitated during the electrolysis of residual water in the DES at highly negative

potentials.[66,71]

The ability of understanding the effect (and controlling the amount) of residual water in a deep eutectic solvent has been proven essential to tune the chemical nature of the electrodeposited Ni nanostructures, thereby, obtaining highly electroactive NPs for a wide range of applications. A thorough understanding of the passivation and the self-limiting growth of metal nanostructures during electrodeposition processes from DESs is essential to reach this aim.

Conclusions

The processes underlying the electrodeposition of nickel nanostructures on carbon substrates from 1:2 ChCl-U are explained in detail by means of the combination of electrochemical techniques and ex-situ nanoscale characterization. A passivation phenomenon is highlighted when electrodeposition occurs at highly negative potentials (E = -1,1 V vs Ag QRE) and is attributed to the presence of residual water in the DES. The splitting of this residual water, catalysed by the presence of nickel, leads to the formation of a mixed layer of Ni/$Ni(OH)_{2(ads)}$ on the surface of the nanostructures. Moreover, the hydroxide species could form hydrogen bonds with the DES molecules (urea and choline chloride), and hence, the growth of Ni NPs is quenched. This allows homogeneous and dense nanoparticle distributions to be electrodeposited within a wide potential range. Furthermore, it is found that anodic polarization immediately after deposition at highly negative potentials results into the inhibition of oxidative electrodissolution of Ni. This anodic passivation process is related to the formation of an entire layer of $Ni(OH)_2$ on the surface of the Ni nanoparticles. These results show that metal electrodeposition from DESs can be of great interest to produce supported nanostructures in a controllable and efficient way and valuable for a broad range of applications and technologies.

Supporting Information Available

The following files are available free of charge.

Charge densities of depositions of figure 2(a).

Low magnification HAADF-STEM images.

Acknowledgements

E.A. Mernissi Cherigui acknowledges funding from the Fonds Wetenschappelijk Onderzoek in Flanders (FWO, research project G019014N). S. Bals acknowledges funding from the European Research Council (Starting Grant No. COLOURATOMS 335078). H.V. gratefully acknowledges financial support by the Flemish Fund for Scientific Research (FWO Vlaanderen). Finally, J. Ustarroz acknowledges funding from the Fonds Wetenschappelijk Onderzoek in Flanders (FWO, postdoctoral grant 12I7816N).

References

(1) Popczun, E. J.; McKone, J. R.; Read, C. G.; Biacchi, A. J.; Wiltrout, A. M.; Lewis, N. S.; Schaak, R. E. Nanostructured nickel phosphide as an electrocatalyst for the hydrogen evolution reaction. *J. Am. Chem. Soc.* **2013**, *135*, 9267–9270.

(2) Morozov, Y. G.; Belousova, O. V.; Kuznetsov, M. V. Preparation of nickel nanoparticles for catalytic applications. *Inorg. Mater.* **2011**, *47*, 36–40.

(3) Chelaghmia, M. L.; Nacef, M.; Affoune, A. M. Ethanol electrooxidation on activated graphite supported platinum-nickel in alkaline medium. *J. Appl. Electrochem.* **2012**, *42*, 819–826.

(4) Metin, Ö. .; Mazumder, V.; Özkar, S.; Sun, S. Monodisperse nickel nanoparticles and

their catalysis in hydrolytic dehydrogenation of ammonia borane. *J. Am. Chem. Soc.* **2010**, *132*, 1468–1469.

(5) Zhang, J.; Chen, C.; Yan, W.; Duan, F.; Zhang, B.; Gao, Z.; Qin, Y. Ni nanoparticles supported on CNTs with excellent activity produced by atomic layer deposition for hydrogen generation from hydrolysis of ammonia borane. *Catal. Sci. Technol.* **2015**, *6*, 2112–2119.

(6) Chase, Z. A.; Kasakov, S.; Shi, H.; Vjunov, A.; Fulton, J. L.; Camaioni, D. M.; Balasubramanian, M.; Zhao, C.; Wang, Y.; Lercher, J. A. State of Supported Nickel Nanoparticles during Catalysis in Aqueous Media. *Chem. - A Eur. J.* **2015**, *21*, 16541–16546.

(7) Mahyari, M.; Shaabani, a. Nickel nanoparticles immobilized on three-dimensional nitrogen-doped graphene as a superb catalyst for the generation of hydrogen from the hydrolysis of ammonia borane. *J. Mater. Chem. A* **2014**, *2*, 16652–16659.

(8) Zhou, L.; Zhang, T.; Tao, Z.; Chen, J. Ni nanoparticles supported on carbon as efficient catalysts for the hydrolysis of ammonia borane. *Nano Res.* **2014**, *7*, 774–781.

(9) Dhokale, R. K.; Yadav, H. M.; Achary, S. N.; Delekar, S. D. Anatase supported nickel nanoparticles for catalytic hydrogenation of 4-nitrophenol. *Appl. Surf. Sci.* **2014**, *303*, 168–174.

(10) Ge, X.; Gu, C. D.; Lu, Y.; Wang, X. L.; Tu, J. P. A versatile protocol for the ionothermal synthesis of nanostructured nickel compounds as energy storage materials from a choline chloride-based ionic liquid. *J. Mater. Chem. A* **2013**, *1*, 13454.

(11) Wang, S.; Wang, J.; Zhu, M.; Bao, X.; Xiao, B.; Su, D.; Li, H.; Wang, Y. Molybdenum-Carbide-Modified Nitrogen-Doped Carbon Vesicle Encapsulating Nickel Nanoparticles: A Highly Efficient, Low-Cost Catalyst for Hydrogen Evolution Reaction. *J. Am. Chem. Soc.* **2015**, *137*, 15753–15759.

(12) Neiva, E. G. C.; Oliveira, M. M.; Marcolino, L. H.; Zarbin, A. J. G. Nickel nanoparticles with hcp structure: Preparation, deposition as thin films and application as electrochemical sensor. *J. Colloid Interface Sci.* **2016**, *468*, 34–41.

(13) Iwamoto, T.; Nagao, A.; Kitagishi, K.; Honjo, S.; Jeyadevan, B. Chemical synthesis of self-assembled Ni nanoparticles and understanding of nonmagnetic layer inside their surface. *J. Phys. Chem. Solids* **2015**, *87*, 136–146.

(14) Chen, L.; Fang, M.; Liu, C.; Liu, X.; Xing, S. Manipulating the nickel shape and catalytic performance: from spheres to chains to urchins. *CrystEngComm* **2015**, *17*, 4343–4348.

(15) Jie, Y.; Fan, H.; Niskala, J. R.; You, W. Growth of nickel nanoparticles on an organic self-assembled monolayer template by means of electroless plating. *Colloids Surfaces A Physicochem. Eng. Asp.* **2013**, *434*, 194–199.

(16) Li, P.; Jiang, W.; Li, F. Non-aqueous sol-gel preparation of carbon-supported nickel nanoparticles. *J. Sol-Gel Sci. Technol.* **2013**, *65*, 359–366.

(17) Chen, T.; Deng, F.; Zhu, J.; Chen, C.; Sun, G.; Ma, S.; Yang, X. Hexagonal and cubic Ni nanocrystals grown on graphene: phase-controlled synthesis, characterization and their enhanced microwave absorption properties. *J. Mater. Chem.* **2012**, *22*, 15190.

(18) Li, G.-R.; Xu, H.; Lu, X.-F.; Feng, J.-X.; Tong, Y.-X.; Su, C.-Y. Electrochemical synthesis of nanostructured materials for electrochemical energy conversion and storage. *Nanoscale* **2013**, *5*, 4056–4069.

(19) Cheng, Q.; Wu, C.; Chen, J.; Zhou, Y.; Wu, K. Electrochemical tuning the activity of nickel nanoparticle and application in sensitive detection of chemical oxygen demand. *J. Phys. Chem. C* **2011**, *115*, 22845–22850.

(20) Bayandori Moghaddam, A.; Ganjali, M. R.; Saboury, A. A.; Moosavi-Movahedi, A. A.; Norouzi, P. Electrodeposition of nickel oxide nanoparticles on glassy carbon surfaces: application to the direct electron transfer of tyrosinase. *J. Appl. Electrochem.* **2008**, *38*, 1233–1239.

(21) Jin, C.; Zeng, A.; Cho, S. J.; Nam, S. H.; Seo, H. O.; Kim, Y. D.; Boo, J. H. Effect of deposition time and potential on the nucleation and growth of nickel nano particles on nitrogen doped diamond-like carbon thin film. *Thin Solid Films* **2012**, *521*, 158–162.

(22) Salimi, A.; Sharifi, E.; Noorbakhsh, A.; Soltanian, S. Direct voltammetry and electrocatalytic properties of hemoglobin immobilized on a glassy carbon electrode modified with nickel oxide nanoparticles. *Electrochem. commun.* **2006**, *8*, 1499–1508.

(23) Salimi, A.; Sharifi, E.; Noorbakhsh, A.; Soltanian, S. Immobilization of glucose oxidase on electrodeposited nickel oxide nanoparticles: Direct electron transfer and electrocatalytic activity. *Biosens. Bioelectron.* **2007**, *22*, 3146–3153.

(24) Gómez, E.; Pollina, R.; Vallés, E. Nickel electrodeposition on different metallic substrates. *J. Electroanal. Chem.* **1995**, *386*, 45–56.

(25) Proud, W. G.; Gomez, E.; Sarret, E.; Valles, E.; Müller, C. Influence of pH on nickel electrodeposition at low nickel(II) concentrations. *J. Appl. Electrochem.* **1995**, *25*, 770–775.

(26) Schlesinger, M.; Paunovic, M. *Modern Electroplating*; Wiley: Hoboken, New Jersey, 2010.

(27) Vanpaemel, J.; van der Veen, M. H.; De Gendt, S.; Vereecken, P. M. Enhanced nucleation of Ni nanoparticles on TiN through H3BO3-mediated growth inhibition. *Electrochim. Acta* **2013**, *109*, 411–418.

(28) Vanpaemel, J.; Sugiura, M.; Cuypers, D.; Van Der Veen, M. H.; De Gendt, S.; Vereecken, P. M. Electrochemical deposition of subnanometer Ni films on TiN. *Langmuir* **2014**, *30*, 2047–2053.

(29) Fukumoto, K.; Yoshizawa, M.; Ohno, H. Room temperature ionic liquids from 20 natural amino acids. *J. Am. Chem. Soc.* **2005**, *127*, 2398–2399.

(30) Zhu, Y.-L.; Katayama, Y.; Miura, T. Electrochemical Preparation of Nickel and Iron Nanoparticles in a Hydrophobic Ionic Liquid. *Electrochem. Solid-State Lett.* **2011**, *14*, D110–D115.

(31) Thomazeau, C.; Olivier-Bourbigou, H.; Magna, L.; Luts, S.; Gilbert, B. Determination of an acidic scale in room temperature ionic liquids. *J. Am. Chem. Soc.* **2003**, *125*, 5264–5265.

(32) Smith, E. L.; Abbott, A. P.; Ryder, K. S. Deep Eutectic Solvents (DESs) and Their Applications. *Chem. Rev.* **2014**, *114*, 11060–11082.

(33) Abbott, A. P.; Capper, G.; Davies, D. L.; McKenzie, K. J.; Obi, S. U. Solubility of metal oxides in deep eutectic solvents based on choline chloride. *J. Chem. Eng. Data* **2006**, *51*, 1280–1282.

(34) Wagle, D. V.; Zhao, H.; Baker, G. A. Deep Eutectic Solvents: Sustainable Media for Nanoscale and Functional Materials. *Acc. Chem. Res.* **2014**, *47*, 2299–2308.

(35) Paiva, A.; Craveiro, R.; Aroso, I.; Martins, M.; Reis, R.; Barreiros, S.; Duarte, A. Natural Deep Eutectic Solvents-Solvents for the 21st Century. *ACS Sustain. Chem. Eng.* **2014**, *2*, 1063–1071.

(36) Nkuku, C. A.; LeSuer, R. J. Electrochemistry in deep eutectic solvents. *J. Phys. Chem. B* **2007**, *111*, 13271–13277.

(37) Du, C.; Zhao, B.; Chen, X.-B.; Birbilis, N.; Yang, H. Effect of water presence on choline chloride-2urea ionic liquid and coating platings from the hydrated ionic liquid. *Sci. Rep.* **2016**, *6*, 29225.

(38) Hammons, J. A.; Muselle, T.; Ustarroz, J.; Tzedaki, M.; Raes, M.; Hubin, A.; Terryn, H. Stability, assembly, and particle/solvent interactions of Pd nanoparticles electrodeposited from a deep eutectic solvent. *J. Phys. Chem. C* **2013**, *117*, 14381–14389.

(39) Bund, A.; Zschippang, E. Nickel Electrodeposition from a Room Temperature Eutectic Melt. *ECS Trans.* **2007**, *3*, 253–261.

(40) Abbott, a. P.; El Ttaib, K.; Ryder, K. S.; Smith, E. L. Electrodeposition of nickel using eutectic based ionic liquids. *Trans. IMF* **2008**, *86*, 234–240.

(41) Abbott, A. P.; Ballantyne, A.; Harris, R. C.; Juma, J. A.; Ryder, K. S. Bright metal coatings from sustainable electrolytes: the effect of molecular additives on electrodeposition of nickel from a deep eutectic solvent. *Phys. Chem. Chem. Phys.* **2017**, *19*, 3219–3231.

(42) Rostom Ali, M.; Rahman, M. Z.; Sankar Saha, S. Electroless and electrolytic deposition of nickel from deep eutectic solvents based on choline chloride. *Indian J. Chem. Technol.* **2014**, *21*, 127–133.

(43) Yang, H.; Guo, X.; Birbilis, N.; Wu, G.; Ding, W. Tailoring nickel coatings via electrodeposition from a eutectic-based ionic liquid doped with nicotinic acid. *Appl. Surf. Sci.* **2011**, *257*, 9094–9102.

(44) Yang, H. Y.; Guo, X. W.; Chen, X. B.; Wang, S. H.; Wu, G. H.; Ding, W. J.; Birbilis, N. On the electrodeposition of nickel-zinc alloys from a eutectic-based ionic liquid. *Electrochim. Acta* **2012**, *63*, 131–138.

(45) Wang, S.; Guo, X.; Yang, H.; Dai, J.; Zhu, R.; Gong, J.; Peng, L.; Ding, W. Electrodeposition mechanism and characterization of Ni-Cu alloy coatings from a eutectic-based ionic liquid. *Appl. Surf. Sci.* **2014**, *288*, 530–536.

(46) Florea, A.; Anicai, L.; Costovici, S.; Golgovici, F.; Visan, T. Ni and Ni alloy coatings electrodeposited from choline chloride-based ionic liquids - Electrochemical synthesis and characterization. *Surf. Interface Anal.* **2010**, *42*, 1271–1275.

(47) Gu, C.; You, Y.; Yu, Y.; Qu, S.; Tu, J. Microstructure, nanoindentation, and electrochemical properties of the nanocrystalline nickel film electrodeposited from choline chloride - ethylene glycol. *Surf. Coatings Technol.* **2011**, *205*, 4928–4933.

(48) Gu, C.; Tu, J. One-step fabrication of nanostructured Ni film with lotus effect from deep eutectic solvent. *Langmuir* **2011**, *27*, 10132–40.

(49) Abbott, A. P.; Ballantyne, A.; Harris, R. C.; Juma, J. A.; Ryder, K. S.; Forrest, G. A Comparative Study of Nickel Electrodeposition Using Deep Eutectic Solvents and Aqueous Solutions. *Electrochim. Acta* **2015**, *176*, 718–726.

(50) Gong, K.; Hua, Y.-x.; Xu, C.-y.; Zhang, Q.-b.; Li, Y.; Ru, J.-j.; Jie, Y.-f. Electrodeposition behavior of bright nickel in air and water-stable betaine·HCl-ethylene glycol ionic liquid. *Trans. Nonferrous Met. Soc. China* **2015**, *25*, 2458–2465.

(51) Abbott, A. P.; Capper, G.; McKenzie, K. J.; Ryder, K. S. Electrodeposition of zinc-tin alloys from deep eutectic solvents based on choline chloride. *J. Electroanal. Chem.* **2007**, *599*, 288–294.

(52) Ustarroz, J.; Gupta, U.; Hubin, A.; Bals, S.; Terryn, H. Electrodeposition of Ag nanoparticles onto carbon coated TEM grids: A direct approach to study early stages of nucleation. *Electrochem. commun.* **2010**, *12*, 1706–1709.

(53) Ustarroz, J.; Altantzis, T.; Hammons, J. a.; Hubin, A.; Bals, S.; Terryn, H. The Role of Nanocluster Aggregation, Coalescence, and Recrystallization in the Electrochemical Deposition of Platinum Nanostructures. *Chem. Mater.* **2014**, *26*, 2396–2406.

(54) Abbott, A.; Barron, J.; Ryder, K. Electrolytic deposition of Zn coatings from ionic liquids based on choline chloride. *Trans. IMF* **2009**, *87*, 201–207.

(55) Ustarroz, J.; Hammons, J. A.; Altantzis, T.; Hubin, A.; Bals, S.; Terryn, H. A generalized electrochemical aggregative growth mechanism. *J. Am. Chem. Soc.* **2013**, *135*, 11550–11561.

(56) Ustarroz, J.; Ke, X.; Hubin, A.; Bals, S.; Terryn, H. New insights into the early stages of nanoparticle electrodeposition. *J. Phys. Chem. C* **2012**, *116*, 2322–2329.

(57) Kim, Y. R.; Lai, S. C. S.; McKelvey, K.; Zhang, G.; Perry, D.; Miller, T. S.; Unwin, P. R. Nucleation and Aggregative Growth of Palladium Nanoparticles on Carbon Electrodes: Experiment and Kinetic Model. *J. Phys. Chem. C* **2015**, *119*, 17389–17397.

(58) Zhao, Y.; E, Y.; Fan, L.; Qiu, Y.; Yang, S. A new route for the electrodeposition of platinum-nickel alloy nanoparticles on multi-walled carbon nanotubes. *Electrochim. Acta* **2007**, *52*, 5873–5878.

(59) Casella, I. G.; Guascito, M. R.; Sannazzaro, M. G. Voltammetric and XPS investigations of nickel hydroxide electrochemically dispersed on gold surface electrodes. *J. Electroanal. Chem.* **1999**, *462*, 202–210.

(60) Luo, X.; Chen, Y.; Yue, G.-H.; Peng, D.-L.; Luo, X. Preparation of hexagonal close-packed nickel nanoparticles via a thermal decomposition approach using nickel acetate tetrahydrate as a precursor. *J. Alloys Compd.* **2009**, *476*, 864–868.

(61) Grosvenor, A. P.; Biesinger, M. C.; Smart, R. S. C.; McIntyre, N. S. New interpretations of XPS spectra of nickel metal and oxides. *Surf. Sci.* **2006**, *600*, 1771–1779.

(62) Marcus, P. *Corrosion Mechanisms in Theory and Practice*; CRC Press: New York, Basel, 2002.

(63) Hall, D. S.; Lockwood, D. J.; Bock, C.; MacDougall, B. R. Nickel hydroxides and related materials: a review of their structures, synthesis and properties. *Proc. R. Soc. A* **2015**, *471*, 20140792.

(64) Hammons, J. A.; Ustarroz, J.; Muselle, T.; Torriero, A. A. J.; Terryn, H.; Suthar, K.; Ilavsky, J. Supported silver nanoparticle and near-interface solution dynamics in a deep eutectic solvent. *J. Phys. Chem. C* **2016**, *120*, 1534–1545.

(65) Liu, Y.; Gokcen, D.; Bertocci, U.; Moffat, T. P. Self-Terminating Growth of Platinum Films by Electrochemical Deposition. *Science* **2012**, *338*, 1327–1330.

(66) Wang, R.; Bertocci, U.; Tan, H.; Bendersky, L. A.; Moffat, T. P. Self-Terminated Electrodeposition of Ni, Co and Fe Ultrathin Films. *J. Phys. Chem. C* **2016**, *120*, 16228–16237.

(67) Ritzert, N. L.; Moffat, T. P. Ultramicroelectrode Studies of Self-Terminated Nickel Electrodeposition and Nickel Hydroxide Formation upon Water Reduction. *J. Phys. Chem. C* **2016**, *120*, 27478–27489.

(68) Oshchepkov, A. G.; Bonnefont, A.; Saveleva, V. A.; Papaefthimiou, V.; Zafeiratos, S.; Pronkin, S. N.; Parmon, V. N.; Savinova, E. R. Exploring the Influence of the Nickel Oxide Species on the Kinetics of Hydrogen Electrode Reactions in Alkaline Media. *Top. Catal.* **2016**, *59*, 1319–1331.

(69) Zeng, K.; Zhang, D. Recent progress in alkaline water electrolysis for hydrogen production and applications. *Prog. Energy Combust. Sci.* **2010**, *36*, 307–326.

(70) Yue, D.; Jia, Y.; Yao, Y.; Sun, J.; Jing, Y. Structure and electrochemical behavior of

ionic liquid analogue based on choline chloride and urea. *Electrochim. Acta* **2012**, *65*, 30–36.

(71) Sharel, P. E.; Liu, D.; Lazenby, R. A.; Sloan, J.; Vidotti, M.; Unwin, P. R.; Macpherson, J. V. Electrodeposition of Nickel Hydroxide Nanoparticles on Carbon Nanotube Electrodes: Correlation of Particle Crystallography with Electrocatalytic Properties. *J. Phys. Chem. C* **2016**, *120*, 16059–16068.

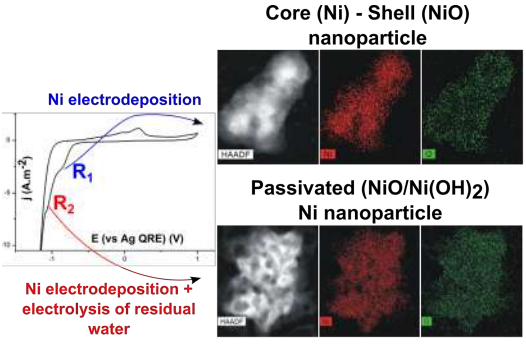
Ni electrodeposition
R1
R2
E (vs Ag QRE) (V)
Ni electrodeposition + electrolysis of residual water
Core (Ni) - Shell (NiO) nanoparticle
HAADF
Ni
O
Passivated (NiO/Ni(OH)2) Ni nanoparticle
HAADF
Ni
O